

In Situ Engineering of Intracellular Hemoglobin for Implantable High-Performance Biofuel Cells

Huifeng Chen⁺, Zhengyu Bai^{+,*}, Xianqi Dai, Xiaoqiao Zeng, Zachary P. Cano, Xiaoxiao Xie, Mingyu Zhao, Matthew Li, He Wang, Zhongwei Chen, Lin Yang,^{*} and Jun Lu^{*}

Abstract: The key challenge for the broad application of implantable biofuel cells (BFCs) is to achieve inorganic–organic composite biocompatibility while improving the activity and selectivity of the catalysts. We have fabricated nanoengineered red blood cells (NERBCs) by an environmentally friendly method by using red blood cells as the raw material and hemoglobin (Hb) embedded with ultrasmall hydroxyapatite (HAP, $\text{Ca}_{10}(\text{PO}_4)_6(\text{OH})_2$) as the functional BFC cathode material. The NERBCs showed greatly enhanced cell performance with high electrocatalytic activity, stability, and selectivity. The NERBCs maintained the original biological properties of the natural cell, while enhancing the catalytic oxygen reduction reaction (ORR) through the interaction between $-\text{OH}$ groups in HAP and the Hb in RBCs. They also enabled direct electron transportation, eliminating the need for an electron-transfer mediator, and showed catalytic inactivity for glucose oxidation, thus potentially enabling the development of separator-free BFCs.

Enzyme biofuel cells (EBFCs)^[1] have attracted considerable attention as micro-^[2] or even nanoscale power^[3] sources for implantable biomedical devices, such as cardiac pacemakers,^[4] implantable self-powered sensors,^[5] and biosensors for monitoring physiological parameters.^[6] There are two types of EBFCs, which differ in the operating mechanism; namely, mediated electron transfer (MET)^[7] and direct electron

transfer (DET)^[8] EBFCs. MET EBFCs rely heavily on redox mediators to shuttle electrons between biocatalytic active sites and electrode surfaces, whereas DET EBFCs enable electron transfer from the enzyme active sites directly to the electrode.^[9] In either case, the other electrode (cathode) requires an oxygen-reduction catalyst, such as laccase^[10] or bilirubin oxide (BOD),^[11] to facilitate the oxygen reduction reaction (ORR). Unfortunately, in general, the current catalysts under investigation show very low catalytic performance as well as poor adhesion to the electrode surface. Such drawbacks drastically limit the practical application of EBFCs.^[12]

Although approaches such as electrode nanomodification,^[1b] enzyme immobilization,^[13] and redox-mediator addition^[14] have been intensively investigated to facilitate electron transfer between enzymes and electrodes, they usually face some challenges, such as avoiding the deformation and inactivation of enzymes,^[15] preventing nanotoxicity,^[16] or improving the stability of the cell.^[17] As is well-known, the biosafety of nanomaterials synthesized in vitro for long-term operation in the body, in other words, the use of invasive, external, and foreign (relative to the nature of the cell) nanomaterials, is controversial, for many reasons, including their unexpected migration and accumulation.^[18] Nanobioengineering,^[19] which has already seen great success in the fields of medicine, agriculture, environment, and electronic systems offers a potential opportunity to tackle these challenges. In situ biomineralization^[20] processes enable the generation of biological materials with special biological functions in vivo, thus offering a promising approach to tune the biofunctionality of materials with good biocompatibility.

Red blood cells (RBCs), which make up nearly 40–45% of blood volume, are responsible for oxygen transport to each body tissue. The hemoglobin (Hb) in RBCs consists of two α - and two β -globins encapsulated by a phospholipid bilayer membrane, each of which has a single heme unit as a prosthetic group. Hb is the iron-containing oxygen-transport metalloprotein, which brings oxygen from the lungs or gills to the rest of the body. Owing to this unique function, RBCs are widely employed in electronic systems, such as biosensors, biological monitoring systems,^[21] and bioelectrocatalysts.^[22] We demonstrate herein the construction of nanoengineered red blood cells (NERBCs) by using the intracellular bonds between the exogenous Ca^{2+} and PO_4^{3-} to generate extremely small hydroxyapatite ($\text{Ca}_{10}(\text{PO}_4)_6(\text{OH})_2$, HAP) particles in situ. The generated NERBCs contain built-in HAP nanodots with a size of approximately 3.1 nm that exhibit strong interaction with Hb owing to the anchored and secured nature of the HAP nanodots, which prevents the

[*] H. Chen,^[†] Z. Bai,^[†] X. Dai, X. Xie, M. Zhao, H. Wang, L. Yang Collaborative Innovation Center of Henan Province for Green Manufacturing of Fine Chemicals, Key Laboratory of Green Chemical Media and Reactions, Ministry of Education, School of Chemistry and Chemical Engineering and College of Physics and Materials Science, Henan Normal University Xixiang, Henan 453007 (P. R. China) E-mail: baizhengyu@htu.cn yanglin@htu.edu.cn

X. Zeng, M. Li, J. Lu
Chemical Sciences and Engineering Division
Argonne National Laboratory
Lemont, IL (USA)
E-mail: junlu@anl.gov

Z. P. Cano, M. Li, Z. Chen
Department of Chemical Engineering, Waterloo Institute for Nanotechnology, Waterloo Institute for Sustainable Energy
University of Waterloo
200 University Avenue West, Waterloo, ON N2L 3G1 (Canada)

[†] H.C. and Z.B. contributed equally to this work and should be considered co-first authors.

Supporting information and the ORCID identification number(s) for the author(s) of this article can be found under <https://doi.org/10.1002/anie.201902073>.

migration and unexpected accumulation of nanodots. Moreover, the overall morphology and biological properties of natural red blood cells, including membrane permeability and longevity, are well preserved. Furthermore, the NERBCs have stronger oxygen-adsorption capacity and show better performance than natural red blood cells, as supported by both experimental results and theoretical calculations. We demonstrate herein that when they are employed as a cathode catalyst for BFCs, they show clear advantages, including increased current density, a long lifetime, high selectivity, and excellent biocompatibility.

The in situ synthesis of NERBCs consisted of two simple processes. Briefly, Ca^{2+} was first added to a solution of RBCs, and the mixture was stirred gently for 1.5 h at 4 °C. This step is important to allow the Ca^{2+} to pass through the cell membrane and effectively reach the interior of RBCs, thus enabling it to combine with Hb. Subsequently, the solution was centrifuged, and the resulting precipitate was washed. In the second step, phosphate buffer solution (PBS, pH 9) was added to the above system, and the mixture was incubated for 2 h at 4 °C, during which PO_4^{3-} and OH^- passed through the RBC cell membrane and entered the cells, thus leading to the generation of the NERBCs.

Scanning electron microscopy (SEM) analysis indicated that the cell morphology was not changed after the synthesis of NERBCs (Figure 1 a, b), thus suggesting that the nanodot formation process did not harm the RBCs. X-ray diffraction (XRD) indicated that the as-synthesized nanoparticles separated from NERBCs were HAP crystals with a hexagonal lattice (Figure 1 c), and transmission electron microscopy (TEM) clearly showed that the intracellular HAP nanodots were polycrystalline (Figure 1 d, inset). Individual intracellular HAP nanodots showed lattice fringe spacing of 0.342 and 0.339 nm (Figure 1 e); these values are in good agreement with the (002) plane of the HAP crystals. The intracellular HAP nanodots were homogeneously dispersed with a uniform size of (3.1 ± 0.1) nm (Figure 1 f). Such extremely small nanodots and uniform dispersion are difficult to achieve by

using other chemical methods and most likely indicate a high acceptance of the nanodots into the RBC structure. These results not only indicate that nanocrystalline HAP was produced in the cells, but also that the generated HAP had excellent biocompatibility.

To determine the interaction between intracellular Hb/ Ca^{2+} and HAP nanodots after the first and second steps of the synthesis, we analyzed the FTIR spectra (see Figure S1 a in the Supporting Information) of pure Hb obtained by hemolysis of native RBCs, Ca^{2+} -Hb separated from Ca^{2+} -RBCs, and intracellular HAP-Hb separated from NERBCs. As compared with the FTIR spectrum of pure Hb, in the spectrum of Ca^{2+} -Hb, the amide I peak position shifted from 1638 to 1646 cm^{-1} , and the amide II peak shifted from 1523 to 1537 cm^{-1} , thus indicating a strong interaction between Ca^{2+} and Hb, which lays the foundation for generating HAP. For HAP-Hb, the amide I and amide II stretch vibrations both shifted to higher wave numbers (1650 and 1540 cm^{-1}), thus indicating that HAP nanodots combined with Hb. Moreover, the vibrational bands at 567, 604, and 1031–1120 cm^{-1} could be assigned to O–P–O antisymmetric bending ν_4 , O–P–O bending ν_4 , and P–O bending ν_3 , respectively. These bands substantiate the existence of HAP, in accordance with the XRD pattern. Thermogravimetric analysis (see Figure S1 b) was performed under an air atmosphere from 20 to 750 °C to detect the content of HAP nanodots inside NERBCs. The major mass losses of NERBCs and native RBCs were observed at 220–550 °C because of the combustion of RBCs. After 550 °C, RBCs were burned out, and the remaining amount of intracellular HAP nanodots was about 5 % of the original weight. In short, this characterization confirmed that HAP nanodots were successfully generated and combined with Hb inside the RBCs.

The formation of HAP nanodots inside the RBCs could be identified by means of intracellular staining of HAP nanodots with tetracycline hydrochloride (Figure 2). Tetracycline hydrochloride can couple with Ca^{2+} to generate green fluorescence under UV light (360–370 nm), thus acting as a fluorescent probe for HAP nanodots. The *z*-axis focal plane of confocal laser scanning microscopy (CLSM) images of NERBCs showed that the green fluorescence followed a pattern of shallow–deep–shallow as the confocal plane changed in the *z*-direction (Figure 2 a–i). This trend indicates that HAP nanodots are synthesized inside NERBCs. As a control, there was no fluorescence signal in native RBCs

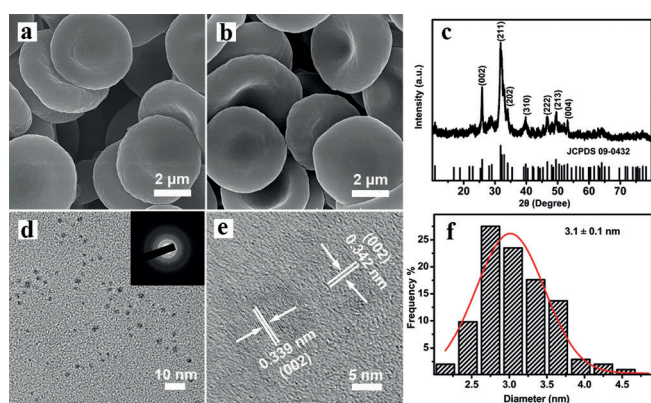


Figure 1. Characterization of HAP nanodots synthesized inside the NERBCs. a) SEM image of NERBCs. b) SEM image of native RBCs. c) XRD of the HAP nanodots separated from the NERBCs. d) TEM image of intracellular HAP nanodots (inset: selected area diffraction of HAP nanodots). e) High-resolution TEM image of several HAP nanodots. f) Particle-size analysis of the HAP nanodots in NERBCs.

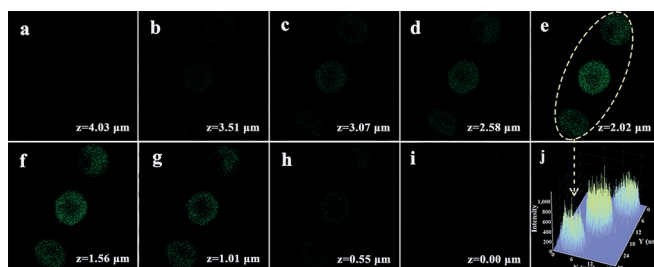


Figure 2. CLSM of the NERBCs labeled with tetracycline hydrochloride. a–i) Different *z*-axis focal planes excited by a 370 nm laser beam. j) 2D mapping of the fluorescence of selected cells.

(see Figure S2), thus manifesting the absence of HAP nanodots in native RBCs. These results indicate that the NERBCs were successfully constructed. 2D mapping of the fluorescence signal of selected NERBCs (Figure 2j) further confirmed that the synthesized HAP nanodots were inside the NERBCs.

Optical images of native RBCs and NERBCs (see Figure S3a,b) showed that the macroscale morphology of NERBCs was exactly the same as that of the native RBCs, and no aggregation was observed. Furthermore, both kinds of cells exhibited good dispersion, although the NERBCs were slightly darker on account of the presence of intracellular HAP nanodots. An osmotic fragility test was carried out to determine the integrity of the cell membrane. The osmotic fragility curve of the NERBCs was nearly identical to that of the native RBCs (Figure 3a), thus indicating that the two

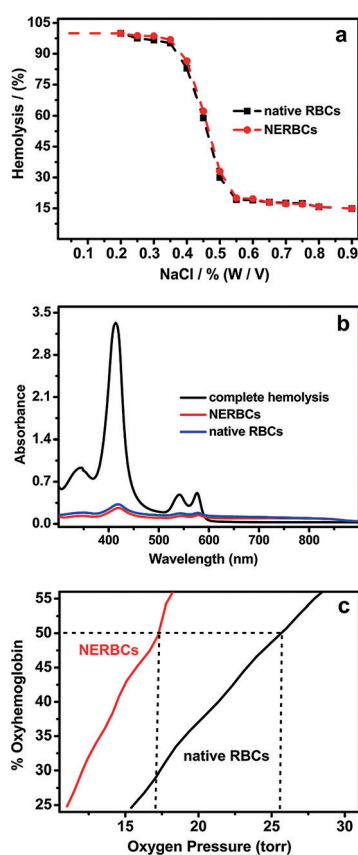


Figure 3. Physical properties of native RBCs and NERBCs. a) Osmotic fragility curves. b) Hemolysis of NERBCs and native RBCs as a control. c) Part of the oxygen equilibrium curves of NERBCs and native RBCs.

kinds of cells shared similar rupture profiles. It is very important to avoid the hemolysis of RBCs because the loss of protection of the cell membrane would cause the Hb to rapidly dissociate into $\alpha\beta$ dimers,^[23] resulting in kidney toxicity. Furthermore, as the prosthetic group of Hb, the free heme has strong toxicity and is destructive to surrounding cells and tissues. Therefore, we also incubated NERBCs in autologous serum to detect any hemolysis. Both native RBCs (blue line) and NERBCs (red line) displayed no clear

hemolysis in fresh autologous serum (Figure 3b), thus demonstrating no evident harmful effect of the synthesis process on the proteins of the membranes after the in situ formation of intracellular HAP nanodots. Hence, our in situ synthesis is mild enough to avoid damage or cause any noticeable change in comparison to the original RBCs, which suggests that the created NERBCs have excellent biocompatibility.

To explore the effect of intracellular HAP nanodots on the oxygen-adsorption capacity of NERBCs, we obtained oxygen equilibrium curves by using a Hemox-Analyzer (TCS Scientific, CA). As compared to native RBCs ($P_{50} = (25.51 \pm 0.56)$ mm Hg), a clear left shift was observed for the NERBCs ($P_{50} = (17.84 \pm 0.63)$ mm Hg; Figure 3c; see also Figure S3c), thus indicating that the Hb oxygen affinity of NERBCs is much higher than that of native RBCs. This phenomenon may be induced by the Bohr effect,^[24] which dictates that as the pH value increases, the affinity of Hb for oxygen increases, causing the oxygen curve to shift to the left.

Electrochemical tests revealed that the NERBCs possessed DET activity and higher electrocatalytic oxygen reduction ability. A pair of well-defined redox peaks were observed at around 0.62 and 0.7 V (vs. RHE) in N_2 -saturated PBS solution containing 4% (v/v) NERBCs (Figure 4a). These Faradaic currents could be due to the Fe^{II}/Fe^{III} redox couple in Hb molecules. The formal potential of the Fe^{II}/Fe^{III} couple of hemoglobin in RBCs was estimated to be 0.66 V (vs. RHE), taken at the midpoint of the redox peaks. These results show that hemoglobin molecules in NERBCs demonstrate DET activity on the bare carboncloth (CC) electrode.

Cyclic voltammetry (CV) measurements of the electrocatalytic ORR activity of native RBCs and NERBCs were carried out in O_2 -saturated PBS solution containing 4% (v/v) of each cell type. Both NERBCs and native RBCs showed an electrochemical reduction response because of abundant O_2 in the PBS solution (Figure 4b). As compared with native RBCs, the reduction peak current of NERBCs increased by about 40%, from 1.92 to 2.67 $mA\ cm^{-2}$. The onset potential of NERBCs was about 0.47 V (Figure 4c), whereas that of native RBCs is about 0.45 V. These data clearly indicate that the NERBCs possess higher electrocatalytic oxygen reduction ability.

CV curves were recorded with different sweep rates from 0.01 to 1 $V\ s^{-1}$ in the PBS solution containing 4% NERBCs (see Figure S4a), and the peak currents were determined by subtracting the non-Faradaic current values. The peak currents were plotted against the sweep rate (see Figure S4b). Since the peak current of CV is proportional to the sweep rate in a surface-controlled process, the observed linear relationship indicates that the bioelectrocatalytic ORR is a surface-controlled process. Furthermore, NERBCs showed much better stability for ORR than RBCs under the same conditions. Figure 4d displays the open-circuit-potential-time (OCP-t) curves. The potential of the half-cell with NERBCs reached a maximum of 0.53 V and continued to rise slowly up to 84 h after initial assembly. In comparison, native RBCs reached a maximum OCP of only 0.42 V, and up to 84 h the OCP value even declined slowly. These results indicate that although RBCs possess stable electrochemical properties, the stability of NERBCs is much better than that of

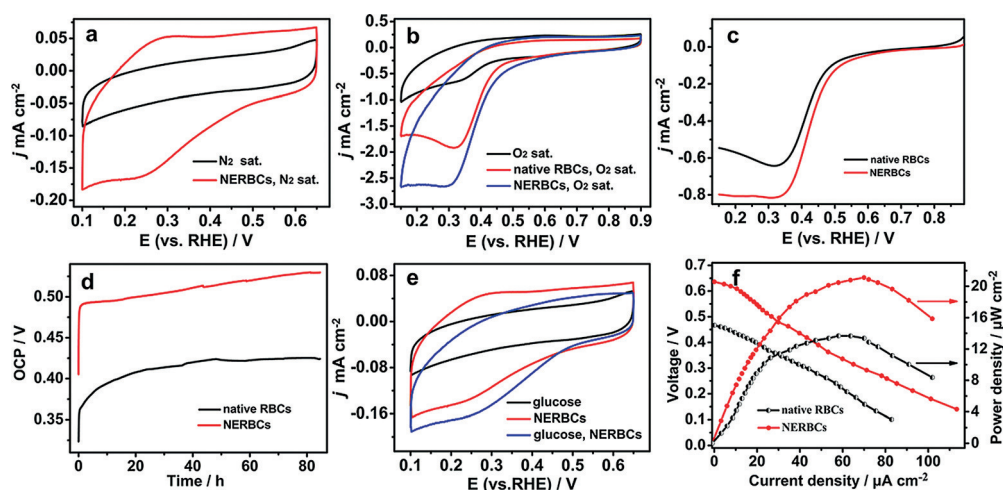
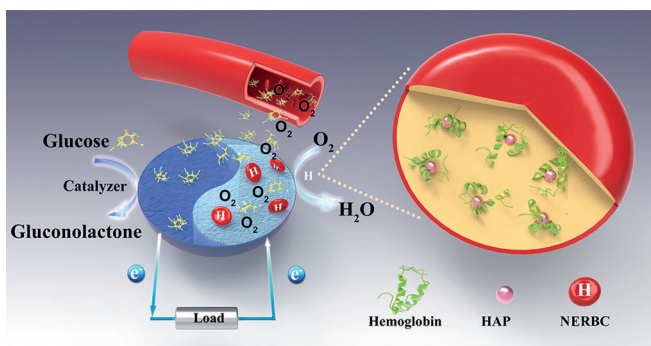


Figure 4. Oxygen reduction reaction electrochemical measurement. a) CV curves of bare CC electrodes in N_2 -saturated PBS ($2\times$, pH 7.4) solution and in N_2 -saturated PBS solution containing 4% NERBCs (v/v), with a sweep rate of 50 mVs^{-1} . b) CV (scan rate: 50 mVs^{-1}) and c) linear sweep voltammetry (LSV) curves (scan rate: 5 mVs^{-1}) of NERBCs and native RBCs in O_2 -saturated PBS solution. d) OCP- t curves of NERBCs and native RBCs acquired under open-circuit conditions in a half-cell. e) CV curves of CC electrodes in N_2 -saturated PBS solution containing 4.5 mM glucose, N_2 -saturated PBS solution containing 4% (v/v) NERBCs, and N_2 -saturated PBS solution containing 4.5 mM glucose and 4% NERBCs (v/v). f) I - V and power characteristics of a single cell composed of an O_2 | NERBCs | CC cathode and a glucose | CC anode.

native RBCs. NERBCs had no evident effect on glucose in N_2 -saturated PBS solution (Figure 4e), which confirms that NERBCs can selectively catalyze ORR.

Subsequently, we simulated the components in the blood to conduct a biological battery test. The performance of a membraneless single cell with an O_2 | RBC | CC biocathode construction (Scheme 1) was measured. The anode was made of glucose as the raw material, and the concentration of the glucose solution used was equal to that of glucose in human blood to ensure relevance and comparability. The observed open-circuit voltage (OCV) of the NERBCs was 0.636 V, and the maximum power density attained was $21.11\ \mu\text{W cm}^{-2}$ (Figure 4f), which are higher than the OCV and power density of native RBCs. The I - V curve and power density confirm that the performance of the BFC equipped with NERBCs is approximately 1.5 times that of native RBCs. These results indicate that the electrocatalytic ORR perfor-



Scheme 1. Assembly diagram of the battery with an O_2 | NERBC | CC biocathode construction.

mance of our designed NERBCs is not only better than that of native RBCs, but is also very competitive with previously reported EBFC ORR catalysts, especially when considering its biocompatibility (see Table S1 in the Supporting Information).

To study the catalytic mechanism of NERBCs, we synthesized RBCs with intracellular CaHPO_4 nanodots (CaHPO_4 @RBCs), which did not contain $-\text{OH}$ groups, as shown by FTIR spectroscopy (see Figure S5). Confocal laser scanning images indicated that CaHPO_4 nanodots were also located inside these RBCs, and were approximately 3.6 nm in diameter (similar to the HAP nanodots). Cyclic voltammetry curves and oxygen equilibrium curves of native RBCs and CaHPO_4 @RBCs were obtained. The bioelectrocatalytic oxygen reduction capability of the CaHPO_4 @RBCs was similar to that of the native RBCs (see Figure S6a). Furthermore, as compared with native RBCs ($P_{50} = (25.51 \pm 0.56)\text{ mm Hg}$), there was a slight left shift of the oxygen curve of CaHPO_4 @RBCs ($P_{50} = (23.37 \pm 0.63)\text{ mm Hg}$) (see Figure S6b). These results indicate that the hemoglobin oxygen affinity of CaHPO_4 @RBCs was in fact almost the same as that of native RBCs. Taken together, these results suggest that the difference in the electrocatalytic activity between CaHPO_4 @RBCs and NERBCs may be due to the absence/presence of $-\text{OH}$ groups.

To further explore the origin of the high electrocatalytic activity of NERBCs, we performed DFT calculations using the (002) surface model of HAP, which was the most stable HAP surface observed according to XRD and TEM measurements (see the Supporting Information for computational details). We calculated the potential-energy (E) surface of the system as the distance ($d_{\text{C-O}}$) between the carbon atom (see Figure S7a) in Hb and $-\text{OH}$ on the HAP surface decreased from 3.35 to $1.46\ \text{\AA}$ (see Figure S7d) and found a value of -0.33 eV for this process, thus indicating that the transfer of $-\text{OH}$ from the center of HAP (002) to the side face of Hb is thermodynamically favored. This transfer enables a strong interaction between the iron center in Hb and oxygen in the presence of the adsorbed $-\text{OH}$, thus weakening the O-O bond and facilitating the O_2 reduction process.

We examined the most stable configuration for Hb adsorption on the HAP (002) surface (see Figure S8a) and the most stable structure for O_2 adsorption on Hb (see Figure S8b). In the latter, the nearest bonding distance between iron and oxygen ($d_{\text{Fe-O}}$) was found to be $1.78\ \text{\AA}$.

However, once the $-OH$ group on the HAP (002) moved to the side face of Hb, the d_{Fe-O} distance was shortened to 1.76 Å. Moreover, Bader charge analysis showed that, before the attachment of the $-OH$ group on Hb (left) there is 0.08e charge transfer between the Fe and O atoms. After the adsorption of $-OH$ on Hb, the corresponding charge transfer between the Fe and O atoms was increased to 0.12e. This observation further confirmed that the enhanced interaction between Fe and the adsorbed O_2 molecule resulted from $-OH$ adsorption on Hb. It is believed that the enhanced interaction between Fe in Hb and O_2 upon $-OH$ adsorption weakens the $O-O$ bond, and thus facilitates O_2 reduction.

In summary, NERBCs were successfully prepared by an in situ synthesis method within the RBCs. This method is based on a mild two-step ion permeation process, in which Hb is combined with Ca^{2+} followed by a phosphate buffer solution (pH 9) containing PO_4^{3-} and OH^- , whereupon HAP nanodots are formed. The formed NERBCs are environmentally friendly, and the product shows excellent biocompatibility with no apparent change in the morphology and permeability relative to the original native RBCs. Their O_2 adsorption ability was greatly enhanced, showing superior stability and ORR electrocatalytic ability with an onset potential of 0.47 V (vs. RHE) and a maximum current density of 2.67 $mA\text{cm}^{-2}$. This study also reveals the advantages of NERBCs as an ORR electrocatalyst with good selectivity and adhesion to the cathode. All the above unique properties could lead to the application of durable, miniature, separator-free BFCs with good biocompatibility. From the experimental results and computational calculations, the superior performance of NERBCs as compared to natural RBCs is due to the controlled formation of HAP through biomineralization. The interaction between the $-OH$ groups in HAP and the Hb in RBCs aids the combination of Fe^{2+} and O_2 , which consequently enhances the adsorption of O_2 . The BFCs based on an O_2 cathode, a glucose anode, NERBCs as the catalyst, and simulated human blood as the electrode exhibited extraordinary performance with an open-circuit voltage of 0.636 V and a maximum energy density of 21.11 μWcm^{-2} . This research provides a promising strategy for the development of novel biocompatible electrocatalysts and offers a new direction for fabricating functional nanoengineered cells.

Acknowledgements

This research was supported by the National Natural Science Foundation of China (Grant No. 21571053 and 51872075), Henan Center for Outstanding Overseas Scientists (Grant No. GZS2018003), the Program for Innovative Research Teams in Science and Technology (Grant No. 18IRTSTHN002, 19IRSTHN023) of the University of Henan Province, and the 111 Project (No. D17007). J.L. gratefully acknowledges support from the U.S. Department of Energy (DOE), Office of Energy Efficiency and Renewable Energy, Vehicle Technologies Office. Argonne National Laboratory is operated for the DOE Office of Science by UChicago Argonne, LLC, under contract number DE-AC02-06CH11357.

Conflict of interest

The authors declare no conflict of interest.

Keywords: electrochemistry · implantable biofuel cells · nanoengineering · oxygen reduction reaction · red blood cells

How to cite: *Angew. Chem. Int. Ed.* **2019**, *58*, 6663–6668
Angew. Chem. **2019**, *131*, 6735–6740

- [1] a) C. H. Kwon, Y. Ko, D. Shin, M. Kwon, J. Park, W. K. Bae, S. W. Lee, J. Cho, *Nat. Commun.* **2018**, *9*, 4479; b) J. Szczesny, N. Marković, F. Conzuelo, S. Zacarias, I. A. Pereira, W. Lubitz, N. Plumeré, W. Schuhmann, A. Ruff, *Nat. Commun.* **2018**, *9*, 4715; c) A. Ruff, J. Szczesny, N. Marković, F. Conzuelo, S. Zacarias, I. A. Pereira, W. Lubitz, W. Schuhmann, *Nat. Commun.* **2018**, *9*, 3675.
- [2] Y. Song, C. Chen, C. J. N. Wang, *Nanoscale* **2015**, *7*, 7084–7090.
- [3] Z. Li, G. Zhu, R. Yang, A. C. Wang, Z. L. Wang, *Adv. Mater.* **2010**, *22*, 2534–2537.
- [4] a) C.-Y. Sue, N.-C. Tsai, *Appl. Energy* **2012**, *93*, 390–403; b) K. MacVittie, J. Halámek, L. Halámková, M. Southcott, W. D. Jemison, R. Lobel, E. Katz, *Energy Environ. Sci.* **2013**, *6*, 81–86.
- [5] A. Zebda, C. Gondran, A. Le Goff, M. Holzinger, P. Cinquin, *Nat. Commun.* **2011**, *2*, 370.
- [6] A. Weltin, J. Kieninger, B. Enderle, A.-K. Gellner, B. Fritsch, *Biosens. Bioelectron.* **2014**, *61*, 192–199.
- [7] a) J. T. Holland, C. Lau, S. Brozik, P. Atanassov, *J. Am. Chem. Soc.* **2011**, *133*, 19262–19265; b) Y. Yamashita, S. Ferri, M. L. Huynh, H. Shimizu, H. Yamaoka, K. Sode, *Enzyme Microb. Technol.* **2013**, *52*, 123–128.
- [8] C.-e. Zhao, P. Gai, R. Song, Y. Chen, J. Zhang, *Chem. Soc. Rev.* **2017**, *46*, 1545–1564.
- [9] S. Calabrese Barton, J. Gallaway, *Chem. Rev.* **2004**, *104*, 4867–4886.
- [10] N. Mano, *Chem. Rev.* **2017**, *118*, 2392–2468.
- [11] J. Filip, A. Andicsová-Eckstein, A. Vikartovská, *Biosens. Bioelectron.* **2017**, *89*, 384–389.
- [12] a) P. Mishra, G. Lakshmi, S. Mishra, D. Avasthi, H. C. Swart, A. P. Turner, Y. K. Mishra, *Nano Energy* **2017**, *39*, 601–607; b) U. Schröder, *Angew. Chem. Int. Ed.* **2012**, *51*, 7370–7372; *Angew. Chem.* **2012**, *124*, 7484–7486.
- [13] a) W. Wang, S. You, X. Gong, D. Qi, B. K. Chandran, L. Bi, F. Cui, X. Chen, *Adv. Mater.* **2016**, *28*, 270–275; b) K. Elouarzaki, D. Cheng, A. C. Fisher, *Nat. Energy* **2018**, *3*, 574–581.
- [14] a) D. Guan, Y. Kurra, W. Liu, Z. Chen, *Chem. Commun.* **2015**, *51*, 2522–2525; b) S. Tsujimura, K. Murata, *J. Am. Chem. Soc.* **2014**, *136*, 14432–14437.
- [15] S. Cosnier, A. J. Gross, A. Le Goff, *J. Power Sources* **2016**, *325*, 252–263.
- [16] F. Durand, C. H. Kjaergaard, E. Suraniti, S. Gounel, R. G. Hadt, E. I. Solomon, *Biosens. Bioelectron.* **2012**, *35*, 140–146.
- [17] E. I. Solomon, P. Chen, M. Metz, S. K. Lee, *Angew. Chem. Int. Ed.* **2001**, *40*, 4570–4590; *Angew. Chem.* **2001**, *113*, 4702–4724.
- [18] a) S. Sharifi, S. Behzadi, S. Laurent, M. L. Forrest, P. Stroeve, *Chem. Soc. Rev.* **2012**, *41*, 2323–2343; b) A. Nel, T. Xia, L. Maedler, N. Li, *Science* **2006**, *311*, 622–627.
- [19] J. R. Bellare, *J. Biomed. Nanotechnol.* **2011**, *7*, 36–37.
- [20] a) X. Ma, H. Chen, L. Yang, K. Wang, Y. Guo, L. Yuan, *Angew. Chem. Int. Ed.* **2011**, *50*, 7414–7417; *Angew. Chem.* **2011**, *123*, 7552–7555; b) B. Wang, C. Zeng, K. H. Chu, D. Wu, H. Y. Yip, L. Ye, *Adv. Energy Mater.* **2017**, *7*, 1700611.
- [21] a) L. Sepunaru, S. V. Sokolov, J. Holter, N. P. Young, *Angew. Chem. Int. Ed.* **2016**, *55*, 9768–9771; *Angew. Chem.* **2016**, *128*, 9920–9923; b) K. Amreen, A. Kumar, *Analyst* **2016**, *141*, 2145–2149.

- [22] Y. Ayato, K. Sakurai, S. Fukunaga, T. Suganuma, K. Yamagiwa, H. Shiroishi, J. Kuwano, *Biosens. Bioelectron.* **2014**, 55, 14–18.
- [23] K. D. Vandegriff, *Exp. Opin. Invest. Drugs* **2000**, 9, 1967–1984.
- [24] G. Di Bella, G. Scandariato, O. Suriano, A. Rizzo, *Science* **1996**, 60, 272–275.

Manuscript received: February 16, 2019

Accepted manuscript online: March 18, 2019

Version of record online: April 9, 2019
